JACS
JOURNAL OF THE AMERICAN CHEMICAL SOCIETY
Article
pubs.acs.org/JACS

Large Enhancements of Thermopower and Carrier Mobility in Quantum Dot Engineered Bulk Semiconductors

Yuanfeng Liu,[†] Pranati Sahoo,[†] Julien P. A. Makongo,[†] Xiaoyuan Zhou,[‡] Sung-Joo Kim,[†] Hang Chi,[‡] Ctirad Uher,[‡] Xiaoqing Pan,[†] and Pierre F. P. Poudeu*,[†]

[†]Department of Materials Science and Engineering and [‡]Department of Physics, University of Michigan, Ann Arbor, 48109, United States

ABSTRACT: The thermopower (S) and electrical conductivity (σ) in conventional semiconductors are coupled adversely through the carriers' density (n) making it difficult to achieve meaningful simultaneous improvements in both electronic properties through doping and/or substitutional chemistry. Here, we demonstrate the effectiveness of coherently embedded full-Heusler (FH) quantum dots (QDs) in tailoring the density, mobility, and effective mass of charge carriers in the n-type $Ti_{0.1}Zr_{0.9}NiSn$ half-Heusler matrix. We propose that the embedded FH QD forms a potential barrier at the interface with the matrix due to the offset of their conduction band minima. This potential barrier discriminates existing charge carriers from the conduction band of the matrix with respect to their relative energy leading to simultaneous large enhancements of the thermopower (up to 200%) and carrier mobility (up to 43%) of the resulting $Ti_{0.1}Zr_{0.9}Ni_{1+x}Sn$ nanocomposites. The improvement in S with increasing mole fraction of the FH-QDs arises from a drastic reduction (up to 250%) in the effective carrier density coupled with an increase in the carrier's effective mass (m*), whereas the surprising enhancement in the mobility (μ) is attributed to an increase in the carrier's relaxation time (τ). This strategy to manipulate the transport behavior of existing ensembles of charge carriers within a bulk semiconductor using QDs is very promising and could pave the way to a new generation of high figure of merit thermoelectric materials.

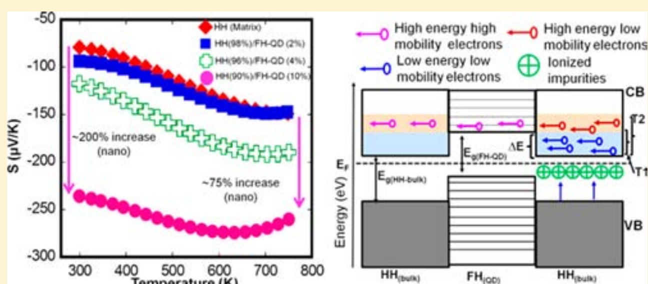

■ INTRODUCTION

Control over the electronic transport properties (thermopower, S; electrical conductivity, σ) of bulk semiconductors has traditionally been achieved by tuning the concentration (n) and mobility (μ) of charge carriers via doping and/or substitutional chemistry. This strategy often results in an increase in the overall density accompanied by a decrease in the mobility of charge carriers within the matrix through the addition of extra charge carriers from the added impurity atoms to the existing free carriers within the matrix. Unfortunately, this alteration of the electronic transport parameters (n, μ) adversely affects the thermopower and electrical conductivity of the matrix. For heavily doped cubic semiconductors, the thermopower (S) and electrical conductivity (σ) can be expressed (within the parabolic band model in the energy-independent scattering approximation) as $S = [(8\pi^2(k_B)^2)/3e\hbar^2]m^*T(\pi/3n)^{2/3}$; and $\sigma = ne\mu$ (k_B is the Boltzmann constant, e is the carrier charge, $\hbar$ is Planck's constant, m^* is the effective mass of the charge carrier, n is the carrier concentration, and μ is the mobility of charge carrier). This interdependence between the thermopower (S) and electrical conductivity (σ) is one of the major roadblocks to the design of thermoelectric materials with a large figure of merit (ZT = $T(\sigma S^2)/\kappa$, where κ is the thermal conductivity, T is the absolute temperature, and σS^2 is the power factor (PF)).[1,2] Therefore, the figures of merit of leading candidate thermoelectric materials are limited to values below ZT ~ 2, despite substantial increases in research activity and innovative breakthroughs in this area over the past decades.[1,3−14] Among various strategies employed to enhance the ZT of traditional and emerging thermoelectric materials, the concept of nanostructuring as an effective means to achieve drastic reductions in the lattice thermal conductivity (κ_L) while minimizing reductions in the PF has dominated thermoelectric research over the past 15 years, and the mechanism by which phonons are scattered at matrix/inclusion interfaces is now better understood.[1,4,5,12,15] The ability to manipulate electronic transport properties (S and σ) within a bulk semiconducting matrix through atomic-scale engineering of the crystal structure of the matrix using nanostructures,[16] rather than the traditional alteration of the chemical composition using substitutional chemistry and/or doping, is a very promising strategy and could pave the way to a new generation of high figure of merit thermoelectric materials designed from current leading candidate material systems. One attractive approach to address this important fundamental problem in thermoelectric research is to find ways to enhance the thermopower (S) and the

Received: November 9, 2012
Published: April 22, 2013

ACS Publications © 2013 American Chemical Society

mobility (μ) of existing free carriers in a semiconducting matrix. This means that the successful strategy must avoid doping the matrix by dumping additional charge carriers to the existing ensemble of free carriers within the matrix.

Since our early reports on the ability to exploit the structural and compositional similarities between the half-Heusler (HH) and full-Heusler (FH) classes of compounds to design novel multifunctional HH/FH nanocomposite materials in which the electronic transport (S, σ) within the HH matrix can be manipulated by engineering its atomic structure using embedded FH nanoinclusions,[11,16] there is a fast growing research interest on the application of similar concept to other thermoelectric materials.[3,17−21] However, the mechanism by which the embedded nanostructures tailor various materials' properties is still poorly understood. HH alloys represent a fascinating large class of intermetallic phases with general composition TMX (T and M are transition or rare-earth metals, and X is a main-group element) and crystallize in the MgAgAs structure type (space group: *F*-43*m*). Their structure can be described as consisting of four interpenetrating face-centered cubic (fcc) sublattices of T, M, and X atoms occupying the crystallographic positions (0,0,0), (1/4, 1/4, 1/4), and (1/2, 1/2,1/2), respectively, whereas the fourth (3/4, 3/4, 3/4) position is vacant.[22,23] Upon filling the empty site, (3/4, 3/4, 3/4), within the structure of a HH (TMX) with an additional M atom, one directly generates the related ternary FH phase with general composition TM_2X (Figure 1).[16] While this

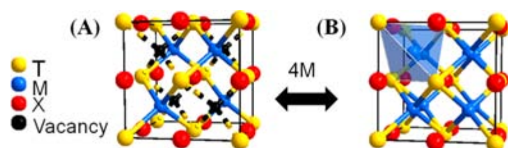

Figure 1. Comparison of the HH and FH crystal structures. (A) HH alloys (TMX) crystallize in the faced centered cubic (fcc) MgAgAs structure type (space group: *F*-43*m*) with half of the tetrahedral position vacant. Upon filling the vacant tetrahedral position with an additional M element, the corresponding FH phase (TM_2X) crystallizing in the cubic $MnCu_2Al$ structure-type (SG: *Fm*-3*m*) is obtained (B).

conversion of a HH structure to the related FH generally induces only a marginal increase (2−5%) in the unit cell parameter, drastic changes in the crystal symmetry occur when switching from the noncentrosymmetric cubic MgAgAs structure type (SG: *F*-43*m*) to the centrosymmetric cubic $MnCu_2Al$ structure type (SG: *Fm*-3*m*). This spontaneous and reversible change in the crystal symmetry upon varying the chemical composition makes the HH and FH compounds, two distinct classes of structurally related materials exhibiting dissimilar physical and chemical properties specific to each class.[11,16,24−43] Although these fascinating two families of compounds have been treated separately over the past several decades, the ability to interchange between the HH and FH structure upon addition or removal of M atoms (at the (3/4, 3/4, 3/4) site) enables the atomic-scale manipulation of the properties (chemical, physical, mechanical, electrical, optical, etc.) of one material by the other. HH alloys play an important role in the search for high-efficiency thermoelectric materials because of their moderate thermopower and electrical resistivity.[28,35] In addition, HH phases are chemically and thermally stable (melting above 1470 K with almost no sublimation at temperatures below 1270 K); they are easy to prepare in large-scale quantities using conventional solid-state synthesis techniques. They also involve cheap, abundant, lightweight, and environmentally friendly elements. These advantages make HH materials suitable for large-scale utilization in high-temperature energy conversion devices.

Here, we show that the thermopower and carrier mobility (μ), within a bulk semiconducting HH matrix with known composition ($Ti_{0.1}Zr_{0.9}$)NiSn (constant carrier density), are gradually enhanced by embedding in a coherent fashion various fractions of FH quantum dots (QDs) within the crystal lattice of the HH matrix. The endotaxial formation of the FH QDs within the HH matrix was confirmed by transmission electron microscopy (TEM) studies. Using electrical conductivity and Hall effect data, we demonstrate the effectiveness of QDs in tailoring the effective charge carrier density, mobility, and effective mass (m^*) within the bulk HH matrix. The concept of carrier culling at the HH/FH QD conduction bands minima offset energy, ΔE, is introduced as a rational mechanism by which the embedded FH QDs alter electronic transport within the HH matrix. A gradual decrease in the effective carrier density and an increase in the effective mass with increasing content of the FH QD resulted in a drastic increase in the thermopower, whereas a simultaneous large increase in the carrier mobility minimizes the drop in the electrical conductivity, leading to an unprecedented enhancement of the PF. This ability to enhance the PF of thermoelectric materials using coherently embedded QDs coupled with the reduction in thermal conductivity via nanostructuring strategy opens up new ways to design atomic-scale structurally engineered counterparts of existing n- and p-type thermoelectric materials with drastically enhanced figures of merit.

■ EXPERIMENTAL SECTION

Synthesis. To fabricate bulk semiconducting HH alloys with integrated metallic FH nanostructures, several alloys with various excess of Ni calculated following the general formula $Ti_{0.1}Zr_{0.9}Ni_{1+x}Sn$ (x = 0, 0.02, 0.04, 0.1) were prepared by direct reaction of stoichiometric amounts (total mass = 5.0 g) of the constituent elements in fused silica ampules. The high-purity elemental powders were thoroughly mixed using an agate mortar and pestle under an inert Ar atmosphere, and the resulting activated powder mixture was then sealed into a quartz tube under a residual pressure of 10^{-4} Torr and subsequently heated at 300 and 900 °C for 3 and 7 days, respectively. Under these synthetic conditions, bulk nanocomposite samples containing various fractions of FH nanoinclusions embedded within the bulk HH matrix were formed accordingly with the chemical eq 1:

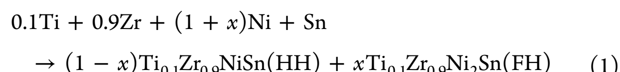

$$0.1Ti + 0.9Zr + (1 + x)Ni + Sn \rightarrow (1 - x)Ti_{0.1}Zr_{0.9}NiSn(HH) + xTi_{0.1}Zr_{0.9}Ni_2Sn(FH) \quad (1)$$

Pellets used for various characterizations were obtained by sintering freshly synthesized polycrystalline powders of HH/FH nanocomposite at 950 °C for 1 h under the applied pressure of 100 MPa using a conventional uniaxial hot press. Detailed densification procedures are described elsewhere.[11,16,24,25] The relative densities of the pressed pellets were obtained by dividing the geometrical density (calculated using the pellet's dimension and mass) by the "true" density of the as-synthesized polycrystalline powder, measured using He gas pycnometry on a Micromeritics Accupyc II 1340. The relative density of all hot pressed pellets was above 95%.

Characterization. The constituent phases of the as-prepared and the sintered materials were evaluated by powder X-ray diffraction on a PANalytical X'pert Pro powder diffractometer operating under 40 kV and 40 mA using a Cu Kα radiation source. The TEM study of selected specimens cut from pressed pellets was performed with JEOL JEM-3011 to probe the size and the distribution of FH nanoinclusions

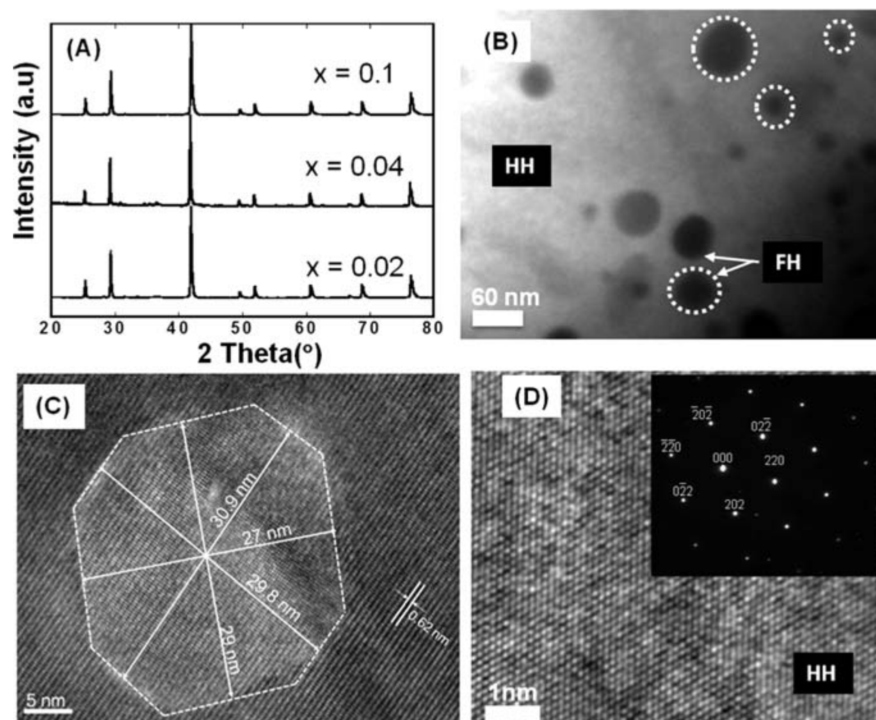

Figure 2. Structural characteristic of $Ti_{0.1}Zr_{0.9}Ni_{1+x}Sn$ nanocomposites. (A) XRD patterns of the as-synthesized $Ti_{0.1}Zr_{0.9}Ni_{1+x}Sn$ materials showing only diffraction peaks of the pure HH phase. No additional peaks corresponding to the anticipated FH secondary phase could be observed. (B) Low-magnification image of the nanocomposite with x = 0.04 showing FH nanoparticles with broad size distribution (10−60 nm) coherently embedded inside the HH ($Ti_{0.1}Zr_{0.9}NiSn$) matrix. (C) High-magnification image of a typical nearly spherical FH nanoparticle (QD) from the nanocomposite with x = 0.1, showing detailed lattice structure. No noticeable strain is observed at the interface between the particle and the matrix, suggesting endotaxial insertion with minimal lattice distortion of the FH particle within the HH matrix. (D) High-magnification image of the HH matrix showing its excellent crystallinity and selected-area electron diffraction pattern (inset of D) indicating the fcc structure of the HH matrix.

embedded within the HH matrix as well as the interface boundary between HH and FH phases. Details on TEM sample preparation are described elsewhere.[11,16,24] The chemical composition of the HH matrix in various HH/FH nanocomposites was carefully analyzed using wavelength dispersive spectroscopy on a Cameca SX-100 electron microprobe analyzer in order to assess the compositional stability of the HH matrix upon addition of excess elemental Ni. Seebeck coefficient and electrical resistivity were measured simultaneously from room temperature to 500 °C under a low pressure He atmosphere using a commercial ZEM-3 system from ULVAC-RIKO. The instrument precision on the electrical resistivity and Seebeck coefficient data is ±4%. The thermal conductivity was calculated from the thermal diffusivity data measured by the laser flash method (LFA-457 from Netzsch) from 20 to 500 °C under flowing N_2 gas (>30 mL/min). The instrument precision on the thermal diffusivity data is ±6%. The electrical conductivity data were combined with the Hall coefficient measurements to evaluate and extract accurate information on the temperature dependence of the carrier density and the mobility of the charge carriers in the nanocomposites. The Hall coefficients data were measured in the temperature range from 300 to 775 K under the magnetic field of 1 T using a large Oxford air-bore superconducting magnet cryostat that accommodates a small tubular oven and a Hall insert. The instrument uncertainty on Hall coefficient data is ±5%.

■ RESULTS AND DISCUSSION

Fabrication and Characterization of QD Engineered HH Semiconductors. Quantum dot (QD) engineered HH semiconducting composite material consisting of $Ti_{0.1}Zr_{0.9}NiSn$ (HH) matrix with various mole fractions of QDs with FH structure (nominal composition $Ti_{0.1}Zr_{0.9}Ni_2Sn$) coherently embedded within the crystal lattice of the HH matrix was achieved by direct solid-state reaction of a mixture of high-purity elemental powders of Zr, Ti, Sn, and Ni in the desired stoichiometry, at 900 °C for 7 days. The mole ratio of Zr, Ti, Ni, and Sn is calculated to form a pure HH phase, and various amounts of excess elemental Ni (0 at. %, 2 at. %, 4 at. %, and 10 at. %) is added to the initial mixture to program a simultaneous partial solid-state transformation of the resulting HH phase into a FH structure according to reaction 1.

Structural characteristics of the resulting $Ti_{0.1}Zr_{0.9}Ni_{1+x}Sn$ nanocomposites were investigated using X-ray powder diffraction (XRD) and transmission electron microscopy (TEM). XRD data (Figure 2A) of the as-synthesized $Ti_{0.1}Zr_{0.9}Ni_{1+x}Sn$ (x = 0.02, 0.04 and 0.1) materials suggested the formation of a single phase HH product as all diffraction peaks were indexed in the cubic MgAgAs structure type (space group: $F\text{-}43m$). No additional peak that could be assigned to the anticipated FH secondary phase or to any other impurity phase could be observed on the diffractions patterns, even for samples with the expected FH mole fraction of up to 10% (x = 0.1). This suggests that according to eq 1, the formation of FH precipitates is on the order of atomic to nanometer scale and does not form aggregates large enough to diffract. Alternatively, the absence of additional peaks on the XRD patterns may indicate the formation of impurity phases that are soluble within the HH matrix. However, the unit cell parameter of the HH matrix in various $Ti_{0.1}Zr_{0.9}Ni_{1+x}Sn$ (x = 0.02, 0.04, and 0.1) materials refined using diffraction peaks from the XRD patterns showed a constant value (Table 1), suggesting that the composition and structure of the HH matrix remain unchanged upon addition of various fractions of excess elemental Ni. To further assess the compositional stability of HH matrix in

Table 1. Wavelength Dispersive Spectroscopy Elemental Analysis of the Matrix Composition in $Ti_{0.1}Zr_{0.9}Ni_{1+x}Sn$ Samples and Unit Cell Parameter of HH Matrix

sample	Ti (at. %)	Zr (at. %)	Ni (at. %)	Sn (at. %)	unit cell parameter (Å)
matrix (x = 0)	1.8	30.3	33.0	34.6	6.095(4)
HH(98%)/FH(2%) (x = 0.02)	1.8	30.7	32.7	34.8	6.115(8)
HH(96%)/FH(4%) (x = 0.04)	1.7	31.0	32.9	34.6	6.098(4)
HH(90%)/FH(10%) (x = 0.1)	1.8	30.5	33.3	34.5	6.104(5)

various $Ti_{0.1}Zr_{0.9}Ni_{1+x}Sn$ (x = 0.02, 0.04, and 0.1) composites, careful analysis of the atomic fraction of Ti, Zr, Ni, and Sn in various specimens was performed using wavelength dispersive spectroscopy. The atomic fraction of various elements (Ti, Zr, Ni, Sn) in each specimen (Table 1) was calculated by averaging 30 data points collected from various locations on the specimens. For each sample, the observed atomic fraction of Ti, Zr, Ni, and Sn is within ±2 at. % of the expected nominal matrix composition (Ti: 3 at. %; Zr: 30 at. %; Ni: 33 at. %; Sn: 33 at. %). The nearly constant values of the atomic fraction of Ti, Zr, Ni, and Sn observed in various specimens strongly indicate that the chemical composition of the HH matrix remains constant in the synthesized $Ti_{0.1}Zr_{0.9}Ni_{1+x}Sn$ composites, in accord with eq 1. To probe the presence of the FH secondary phase within the synthesized nanocomposites and also to determine their characteristics (average size, size distribution, and morphology), high-resolution transmission electron microscopy (HRTEM) study was performed on selected specimens. TEM images from the sample containing 4 at. % excess Ni ($Ti_{0.1}Zr_{0.9}Ni_{1.04}Sn$), which corresponds to a nanocomposite system consisting of 96 mol % HH and 4 mol % FH (96%HH/4%FH), reveal that the FH precipitates have nearly spherical morphology with size ranging from 10 to 60 nm (Figure 2B). The spherical shape of the nanodots suggests endotaxial nucleation of the precipitate seed crystals within the HH crystal lattice followed by their isotropic growth. Careful inspection of a high-magnification image of a typical nanoparticle (Figure 2C) from the sample with an 10 at. % excess Ni ($Ti_{0.1}Zr_{0.9}Ni_{1.1}Sn$) reveals that the precipitates are single crystalline spherical particles with average diameter of ~29 nm. No noticeable strain was observed at the phase boundary between the particle and the HH matrix. The absence of strained domains at the matrix/inclusion interface suggests close structural relationships (e.g., similarity in the lattice constant) between both phases as well as a high level of coherency between lattice planes in both crystals. High-magnification TEM images of a portion of the HH matrix (Figure 2C,D) showed its excellent crystallinity with lattice parameter of ~0.62 nm and selected-area electron diffraction pattern (Figure 2D, inset of D) confirmed that it is a fcc structure. Therefore, we predict based on the above structural details as well as on the chemical eq 1 that the observed precipitates are FH nanodots (QDs). Observation of spherical shaped FH nanodots and their high lattice coherency with the HH matrix suggests a conucleation and growth of both HH and FH seed crystals during the solid-state reaction from the mixture of elemental powers. Under this synthesis condition, high similarity in the composition and atomic arrangement within the HH and FH structures favors competing formation of the two phases. Therefore, the composition and structure (FH or HH) of seed crystals nucleating at various locations within the reaction mixture depend on the local stoichiometry (Zr:Ti:Ni:Sn ratio). The volume fraction of seed crystals with FH structure and composition depend on the amount of excess Ni (x) used in the starting mixture. Because only a small excess of Ni (x = 2%, 4%, and 10%) was used in this study, the largest fraction of seed crystals nucleating in the reaction mixture is of the HH structure. Therefore, large grains with HH structure containing small domains with FH structure coherently embedded in the HH grain are expected. The formation of such HH/FH composites grains likely arises from the merging of several neighboring seed crystals with HH composition and structure surrounding a small fraction of seed crystals with FH composition and structure. This growth mechanism is facilitated by the three-dimensional structural similarity between the FH and HH structure which also favors endotaxial growth of spherically shaped FH inclusions within the HH matrix, leading to the formation of coherent HH/FH interfaces within the composites. This formation mechanism is consistent with the characteristics of the precipitates observed from TEM studies. The final size and dispersion of the FH inclusions within individual grains of the polycrystalline powder of HH/FH composite strongly depend on the population density of FH seed crystals as well as their proximity within the reaction mixture. Because of the relatively facile interchange between HH and FH structures through solid-state Ni diffusion into available vacant sites of the HH structure (Figure 1), the concentration gradient of Ni atoms between FH seed crystals and the surrounding HH crystals as well as the large number of available vacant sites in the HH crystals is likely the driving force for Ni diffusion within individual grains of the HH/FH composite. Through this Ni diffusion process, small unstable FH seed crystals within an individual grain of the HH/FH composites, separated by relatively short distances, can migrate and merge into larger and more stable FH particles (Figure 2B). This conucleation and growth mechanism can therefore lead to HH/FH composite grains in which FH inclusions with sizes as small as 2−3 nm (3−5 unit cells of FH) are coherently integrated within the surrounding HH matrix. The resulting highly coherent atomic-scale phase boundaries between the HH matrix and the FH inclusion allow a close crystallographic registry between both structures. These coherent phase boundaries between the matrix and inclusion phases (Figure 2C) are expected to promote the transfer of charge carriers across the matrix/inclusion interfaces.

Electronic Transports in QD Engineered HH Semiconductors. *Carrier Density.* Figure 3A−D shows the high-temperature electronic transport properties of $Ti_{0.1}Zr_{0.9}NiSn$ (HH) materials containing various mole fractions of the FH nanostructures embedded within the HH matrix. At 300 K, the density of charge carriers in the $Ti_{0.1}Zr_{0.9}NiSn$ (HH) matrix is $\sim 6 \times 10^{19}/cm^3$ (Figure 3A). This value of the carrier density decreases to $\sim 5.2\times 10^{19}/cm^3$ at 300 K, upon addition of 2 at. % excess elemental Ni in the starting mixture, which corresponds to the formation of $Ti_{0.1}Zr_{0.9}Ni_{1.02}Sn$ bulk nanocomposite containing 98 mol % HH and 2 mol % FH (98%HH/2%FH) according to eq 1. Increasing the excess of elemental Ni to 4 at. % results in a larger decrease of the carrier density (57%) at 300

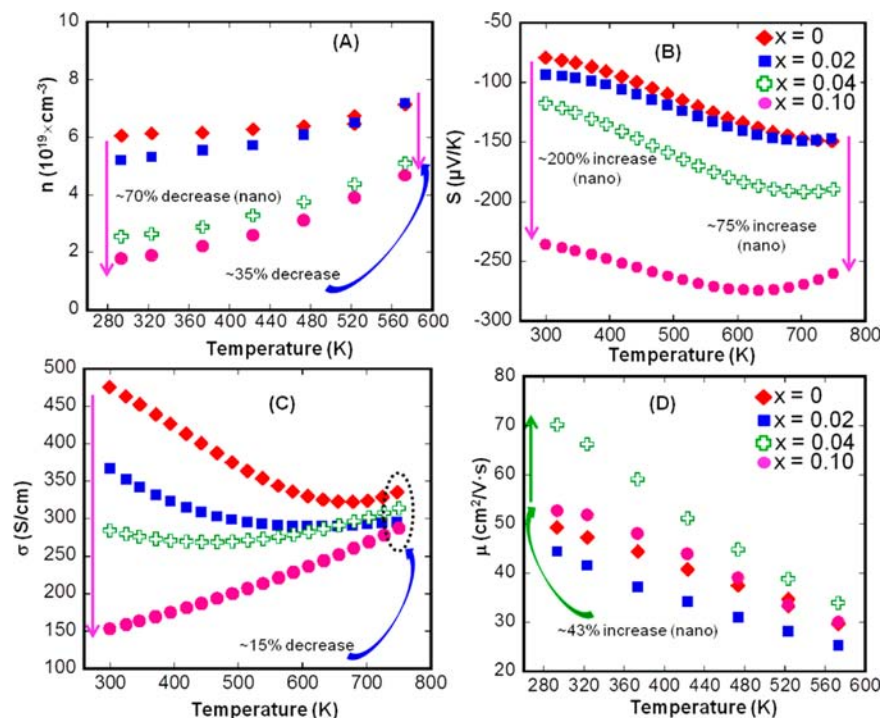

Figure 3. Temperature-dependent electronic transports in QDs engineered $Ti_{0.1}Zr_{0.9}Ni_{1+x}Sn$ nanocomposites. (A) Carrier density; (B) thermopower; (C) electrical conductivity; and (D) carrier mobility.

K within the corresponding 96%HH/4%FH nanocomposites. In the 90%HH/10%FH, a 70% reduction in the carrier density is observed at 300 K when compared to that of the pristine of $Ti_{0.1}Zr_{0.9}NiSn$ (HH) matrix. Careful analysis of temperature-dependent carrier density curves for various $Ti_{0.1}Zr_{0.9}Ni_{1+x}Sn$ (HH($1-x$)/FH(x)) nanocomposites revealed some differences in their shape. For the nanostructure-free composition (x = 0), the carrier density remains almost constant up to 550 K. This behavior is typical for extrinsic semiconductors. As the content of FH nanoinclusion increases, the carrier density becomes progressively more temperature dependent. It should be noted that, regardless of the temperature, the carrier density within the (HH($1-x$)/FH(x)) nanocomposites remains lower or equal to the $Ti_{0.1}Zr_{0.9}NiSn$ (HH) matrix carrier density. Although the gradual increase in the carrier density with temperature observed for the (HH($1-x$)/FH(x)) nanocomposites is similar to the behavior typically expected for doped semiconductors, the fact that the overall carrier density within the HH($1-x$)/FH(x)) nanocomposites at a given temperature remains lower than that of the $Ti_{0.1}Zr_{0.9}NiSn$ (HH) matrix indicates that no additional carriers were added to the existing ensemble of carriers within the $Ti_{0.1}Zr_{0.9}NiSn$ (HH) matrix upon embedding the FH nanostructures. Such reductions in the carrier concentration of the HH/FH composite could be associated with a gradual increase in the band gap of the HH matrix with increasing FH content. However, this simple explanation is not consistent with the thermopower data in which the gradual decrease in the temperature of maximum thermopower with increasing FH content suggests a reduction in the band gap of the HH matrix (Figure 3B). Therefore, the traditional doping concept is not applicable in this system, and an alternative mechanism that accurately describes the observed data must be explored.

The systematic gradual decrease in the carrier density in $Ti_{0.1}Zr_{0.9}Ni_{1+x}Sn$ (HH($1-x$)/FH(x)) nanocomposites with increasing mole fraction of the FH phase is quite surprising. It is well-known that the introduction of large metallic inhomogeneities such as FH phases into a semiconductor such as the HH alloys generally leads to electronic doping of the semiconducting HH matrix by the FH inclusion phase resulting in drastic increases in the carrier density.[16] However, the observed decrease in the carrier density in $Ti_{0.1}Zr_{0.9}Ni_{1+x}Sn$ (HH($1-x$)/FH(x)) nanocomposites with increasing mole fraction of FH inclusions is consistent with our recent results from the Bi-doped HH($1-x$)/FH(x) ($0 \le x \le 0.1$) (HH = $Zr_{0.25}Hf_{0.75}NiSn_{0.975}Bi_{0.025}$) systems.[11] Drop in the carrier density with the increasing FH content in Bi-doped HH($1-x$)/FH(x) ($0 \le x \le 0.1$) was ascribed to the formation of energy barriers, ΔE, at the HH-matrix/FH-inclusion interfaces, which act as an energy filter for conduction electrons within the HH matrix.[11] Here, we use a similar mechanism to rationalize the electronic transport data observed in $Ti_{0.1}Zr_{0.9}Ni_{1+x}Sn$ nanocomposites. The gradual increase in the carrier density with temperature observed in the HH($1-x$)/FH(x)) nanocomposites can be associated with some form of charge carriers "culling" within the conduction band (CB) of the $Ti_{0.1}Zr_{0.9}NiSn$ (HH) matrix, based on their relative energy distribution (e.g., low energy carrier versus high energy carrier), using the embedded FH nanostructures.

As depicted in Figure 4A, the band structure of the FH phase is related to that of the HH phase with similar chemical composition and only differs by the presence of a partially filled band with Ni character on top of the FH valence band (VB). This additional partially filled band pushes the valence band maxima (VBM) and the conduction band minima (CBM) of the FH inclusion to higher energy compared to that of the corresponding HH phase. Therefore, one can anticipate the formation of a type −II (staggered gap) heterojunctions at the nanometer scale HH/FH interfaces within the $Ti_{0.1}Zr_{0.9}Ni_{1+x}Sn$ (HH($1-x$)/FH(x)) nanocomposites (Figure 4B). The energy

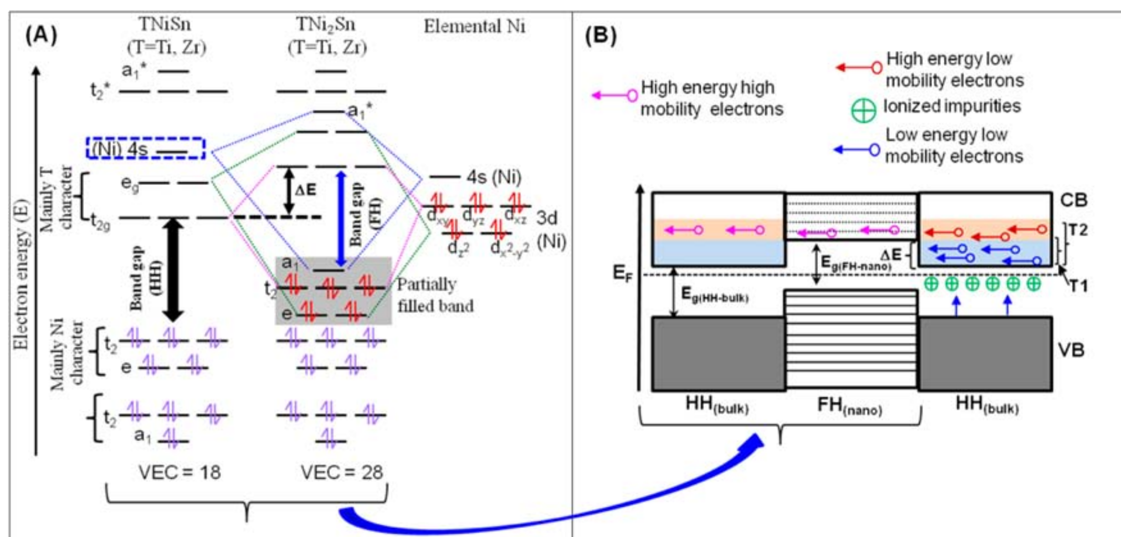

Figure 4. Illustrations of the HH and FH band structures alignment at the HH/FH interfaces. (A) Molecular orbital diagram of FH (TNi_2Sn) generated from that of HH phase (TNiSn) upon insertion of elemental Ni into vacant tetrahedral site. Comparison of the HH and FH molecular orbital diagrams reveals energy offset of both the valence band maxima (VBM) and the conduction band minima (CBM) leading to nanometer scale type-II (staggered gap) heterojunctions at the HH/FH interface. The conduction band energy offset, ΔE, acts as an energy filter for conduction electrons within the HH matrix. (B) Proposed mechanism of the filtering of low energy electrons (from CB of HH) at the potential barrier, ΔE, (reducing effective carrier density) and spatial separation of high energy electrons (within CB of FH) from ionized-impurities at nanometer scale HH/FH heterojunctions. Cyan and orange colors represent distributions of low and high energy electrons at temperatures T1 and T2 (T2 > T1) within the CB of the HH matrix.

offset, ΔE, between CBM in both the HH and FH phases acts as an energy filter for conduction electrons within the CB of the HH matrix. The height of the energy barrier, ΔE, depends on the position of the CBM of the FH inclusion, which in turn, under quantum confinement regime, depends on the size of the FH nanoinclusion. Therefore, the relative reductions in carrier density measured in various $Ti_{0.1}Zr_{0.9}Ni_{1+x}Sn$ (HH(1 − x)/FH(x)) nanocomposites at 300 K correspond to the fraction of low energy conduction electrons from the CB of the HH matrix trapped by the potential barrier, ΔE, at the HH/FH interfaces. The gradual increase in the carrier density with temperature observed in $Ti_{0.1}Zr_{0.9}Ni_{1+x}Sn$ (HH(1 − x)/FH(x)) nanocomposites can thus be attributed to "low energy"(LE) carriers, which are trapped at the energy barrier around 300K, gradually overcoming the ΔE potential barrier due to thermal excitation. The fraction of LE electrons trapped by the potential barrier increases with the population density of HH/FH interfaces within the $Ti_{0.1}Zr_{0.9}Ni_{1+x}Sn$ (HH(1 − x)/FH(x)) nanocomposites, but also decreases with the increasing size of FH nanostructures (decreasing ΔE). Under our synthesis conditions, increasing the percentage of excess elemental Ni atoms in the starting compositions can lead to the formation of: (1) a large number of small FH QDs with narrow size distribution or (2) a mixture of small and large FH QDs. This explains the observed irregularities in the drops of carrier density within the $Ti_{0.1}Zr_{0.9}Ni_{1+x}Sn$ (HH(1 − x)/FH(x)) nanocomposites when going from the 4 at. % excess elemental Ni to the compositions with 10 at. % excess Ni (Figure 3A).

Thermopower. The above-described FH QDs that induce changes in the effective carrier density within the $Ti_{0.1}Zr_{0.9}NiSn$ (HH) matrix as well as their temperature dependence, are also expected to result in large alterations of the thermopower of $Ti_{0.1}Zr_{0.9}Ni_{1+x}Sn$ (HH(1 − x)/FH(x)) nanocomposites (Figure 3B). All $Ti_{0.1}Zr_{0.9}Ni_{1+x}Sn$ (HH(1 − x)/FH(x)) nanocomposites showed negative values of the thermopower in the measured temperature range, suggesting electrons as the majority charge carriers. At 300 K, the thermopower values of $Ti_{0.1}Zr_{0.9}Ni_{1+x}Sn$ nanocomposites increase from −78 μV/K (for x = 0) to −94 μV/K (for x = 0.02). This corresponds to about 20% increase in the thermopower of HH(98%)/FH(2%) nanocomposite compared to the $Ti_{0.1}Zr_{0.9}NiSn$ (HH) matrix. The room temperature values of the thermopower further increase to −118 μV/K (for x = 0.04) and −235 μV/K (for x = 0.1), which correspond to ~50% and ~200% enhancements, respectively, when compared to the thermopower value of the $Ti_{0.1}Zr_{0.9}NiSn$ (HH) matrix at 300K. Regardless of the composition, the absolute values of the thermopower of $Ti_{0.1}Zr_{0.9}Ni_{1+x}Sn$ nanocomposites increase with rising temperature, reaching maximum values at 775K (x = 0), 700K (x = 0.04), and 600K (x = 0.1) and slowly decrease thereafter with further increase in temperature. Although the observed increase in the thermopower with increasing mole fraction of FH content seems to be consistent with the decreasing carrier density, the decrease in the temperature of maximum thermopower of the $Ti_{0.1}Zr_{0.9}Ni_{1+x}Sn$ nanocomposites with increasing FH content suggests a decrease in the band gap which should normally lead to an increase in the carrier density. In addition, careful examination of both the temperature dependent carrier density (Figure 3A) and thermopower (Figure 3B) plots revealed anomalous changes in the magnitude of the thermopower upon altering the carrier density within the $Ti_{0.1}Zr_{0.9}Ni_{1+x}Sn$ (HH(1 − x)/FH(x)) nanocomposites using FH QDs. For instance, the thermopower value of HH(90%)/FH(10%) nanocomposite (x = 0.1) at 300K is twice that of the HH(96%)/FH(4%) nanocomposite, despite their very similar carrier density. This behavior is maintained regardless of the temperature. Also, it is observed that the thermopower value of the HH(98%)/FH(2%) nanocomposite at 700K is almost equal to that of the

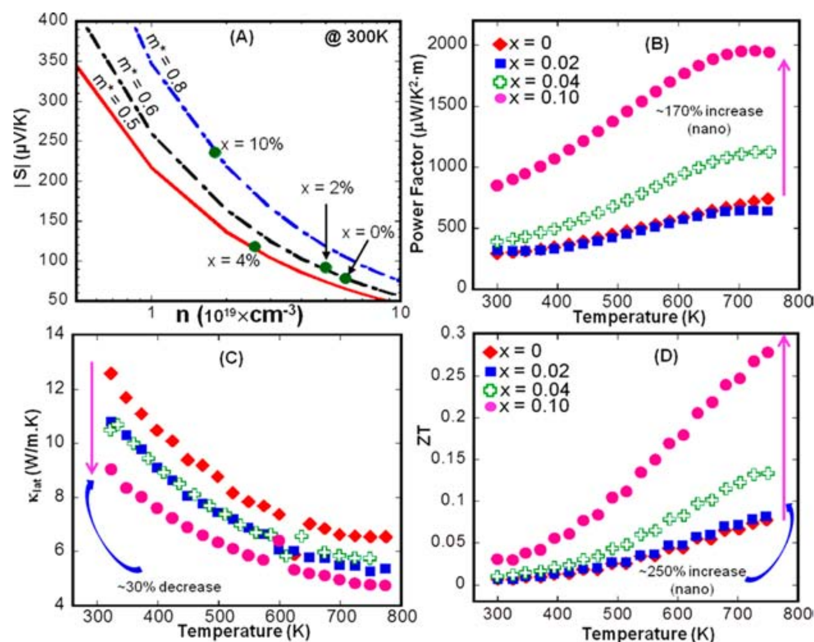

Figure 5. Pisarenko plot and temperature dependence of the thermoelectric performance of $Ti_{0.1}Zr_{0.9}Ni_{1+x}Sn$ nanocomposites. (A) Pisarenko plot showing large enhancements of the thermopower (S) due to simultaneous decrease in carrier concentration and increase in the carrier effective mass (m^*) with increasing excess Ni. Temperature-dependent (B) power factor; (C) lattice thermal conductivity; and (D) thermoelectric figure of merit (ZT) of HH($1 - x$)/FH(x) bulk nanocomposites (x = 0, 0.02, 0.04, and 0.1).

$Ti_{0.1}Zr_{0.9}NiSn$ (HH) matrix despite the noticeable difference in their carrier density at the same temperature.

To fully understand these surprising changes in the thermopower upon alteration of the effective carrier density of the $Ti_{0.1}Zr_{0.9}Ni_{1+x}Sn$ (HH($1 - x$)/FH(x)) nanocomposites using FH QDs, we have constructed Pisarenko plots describing the relationship between the thermopower and carrier density for each of the $Ti_{0.1}Zr_{0.9}Ni_{1+x}Sn$ (HH($1 - x$)/FH(x)) nanocomposites, $S = [(8\pi^2(k_B)^2)/3e\hbar^2]\mathrm{m}^*\mathrm{T}(\pi/3n)^{2/3}$ (k_B is the Boltzmann constant, e is the carrier charge, $\hbar$ is the Planck's constant, m^* is the effective mass of the charge carrier, T is the absolute temperature, n is the carrier concentration), assuming parabolic bands and an energy-independent relaxation time (Figure 5A).[44] Under these assumptions, the thermopower at a given temperature can be described by a unique value of the effective mass (m^*). Figure 5A shows the Pisarenko plots (S versus n) at 300 K for various $Ti_{0.1}Zr_{0.9}Ni_{1+x}Sn$ (HH($1 - x$)/FH(x)) nanocomposites. No single value of the effective mass that allows fitting of all the data could be obtained, suggesting that the embedded FH QDs, in addition to reducing the effective carrier density within the $Ti_{0.1}Zr_{0.9}NiSn$ (HH) matrix, also significantly alter its electronic band structure close to the Fermi level. This is confirmed by large variations in the carrier effective mass (m^*) values extracted from the fitting of $S(n)$ curves under the approximation of the parabolic bands and an energy-independent relaxation time for each $Ti_{0.1}Zr_{0.9}Ni_{1+x}Sn$ (HH($1 - x$)/FH(x)) nanocomposite. At 300 K, the values of the effective mass are m^* = 0.6, 0.62, 0.5, and 0.8 for $Ti_{0.1}Zr_{0.9}Ni_{1+x}Sn$ (HH($1 - x$)/FH(x)) nanocomposite with x = 0, 0.02, 0.04, and 0.1, respectively (Figure 5A). The observed changes in the carrier effective mass (m^*) with increasing mole fraction of FH QDs in the $Ti_{0.1}Zr_{0.9}NiSn$ (HH) matrix explain very well the large difference between the thermopower values of the HH(90%)/FH(10%) (x = 0.1) and HH(96%)/FH(4%) (x = 0.04) nanocomposites, despite their very similar carrier density.

An increase in the effective mass is generally associated with an increase in the energy band gap, E_g.[45] Indeed, the plot of the temperature-dependent carrier density of various $Ti_{0.1}Zr_{0.9}Ni_{1+x}Sn$ (HH($1 - x$)/FH(x)) nanocomposites suggests the presence of a potential barrier (ΔE) at the HH/FH interfaces, and the trapped electrons must now gain sufficient energy to overcome this barrier in order to participate in the electrical conduction. The addition of the potential barrier ΔE corresponds to an increase in the band gap of the HH/QD nanocomposites compared to the HH matrix, since an electron from the valence band (VB) of the HH matrix will now need higher thermal energy to overcome both the intrinsic energy gap (E_g) of the pristine HH matrix and the added potential barrier (ΔE), in order to contribute to the electrical conduction. Therefore, the "apparent" band gap of the HH/QD nanocomposite can be expressed as $E_{g(HH/QD)} = E_{(CBM\text{-}QD)} - E_{(VBM\text{-}HH)} = E_{g(HH)} + \Delta E$, where $E_{(CBM\text{-}QD)}$ and $E_{(VBM\text{-}HH)}$ are the energies of the conduction band minima for the FH QD and the valence band maxima for the HH matrix. Noting that the decrease in the thermopower of various $Ti_{0.1}Zr_{0.9}Ni_{1+x}Sn$ nanocomposites at high temperatures can be ascribed to electron−hole compensation arising from thermal excitation of electrons from the valence band (VB) to the conduction band (CB) of the HH matrix, a reduction in the temperature of maximum thermopower of $Ti_{0.1}Zr_{0.9}Ni_{1+x}Sn$ nanocomposites with increasing FH content suggests a reduction in the band gap, which is not in accord with the observed change in the carrier density. A possible explanation of this anomalous behavior is a thermal excitation of electrons from the VB to the CB within the FH inclusions that occur at lower temperature as the size of the FH inclusion increases. For instance, an increase in the excess of elemental Ni in the HH matrix can result in the formation of a large number of FH inclusions with a slightly larger average size. The increase in the size of the FH inclusions corresponds to a decrease in the band gap of the FH inclusion

and therefore reduction in the energy required to excite electrons from the VB to the CB of FH.

From the analysis above, one can conclude that embedding FH QDs into a semiconducting HH matrix results in a new material with distinct electronic band structure, when compared to that of the HH matrix. The electronic characteristics (e.g., band gap, carrier density, and carrier effective mass) of the resulting HH($1 - x$)/FH(x) material strongly depend on the mole fraction, average size, and distribution for FH QDs within the semiconducting HH matrix. The drastic positive changes in the electronic properties (S, n, and m^*) of the bulk HH matrix, associated with the atomic-scale integration of FH QDs, sharply discriminate this novel method of enhancing the electronic transport of a bulk semiconducting matrix from the traditional doping strategy, where the alteration of carrier density generally maintains the carrier effective mass more or less constant. The ability to simultaneously decrease the carrier density and increase the carrier effective mass within the $Ti_{0.1}Zr_{0.9}NiSn$ (HH) matrix using FH QDs leads to thermopower enhancements superior in magnitude compared to values expected from similar alteration in the carrier density using simple doping methods (Figure 5A).

Carrier Mobility. The mobility of charge carriers in a conventional semiconductor is related to the relaxation time, τ, between scattering events (phonon−electron, ionized-impurity, and electron−electron scattering, etc.) and the carrier effective mass (m^*) by the equation $\mu = e(\tau/m^*)$. Therefore, the above-described alteration of the effective mass of the HH matrix upon embedding the FH QDs is expected to significantly alter the carrier mobility within the resulting $Ti_{0.1}Zr_{0.9}Ni_{1+x}Sn$ (HH($1 - x$)/FH(x)) nanocomposites (Figure 3D). Assuming constant relaxation time, τ, the carrier mobility μ_i in various $Ti_{0.1}Zr_{0.9}Ni_{1+x}Sn$ (HH($1 - x$)/FH(x)) nanocomposites can be related to the carrier mobility μ_0 in the HH matrix by the simple relation $\mu_i = \mu_0$ (m^*_0/m^*_i) (m^*_0 is the carrier effective mass in the HH matrix and m^*_i is the carrier effective mass in a given (HH($1 - x$)/FH(x)) nanocomposite). At 300 K, the carrier mobility slightly decreases from μ_0 = 50 $cm^2/V{\cdot}s$ for the $Ti_{0.1}Zr_{0.9}NiSn$ (HH) matrix to μ_i = 45 $cm^2/V{\cdot}s$ for the HH(98%)/FH(2%) nanocomposite. This 10% reduction in the mobility can be associated with the small increase in the carrier effective mass in the HH(98%)/FH(2%) sample, assuming a constant relaxation time, τ. Upon increasing the mole fraction of FH QDs to $x = 0.04$, the carrier mobility in the resulting HH(96%)/FH(4%) nanocomposite drastically increases to 70 $cm^2/V{\cdot}s$. The observed carrier mobility is 16% larger than the value μ_i = 60 $cm^2/V{\cdot}s$ expected for constant relaxation approximation. Therefore, the observed large increase in the carrier mobility within the HH(96%)/FH(4%) nanocomposite can be attributed to both an increase in the relaxation time and a reduction in the carrier effective mass (Figure 5A). Further increase in the mole fraction of FH QDs to $x = 0.1$ results in a reduction of the room temperature value of the carrier mobility to 53 $cm^2/V{\cdot}s$ due to a large increase in the carrier effective mass ($m^* = 0.8$). However, the observed carrier mobility in the HH(90%)/FH(10%) nanocomposite is still 41% higher than the μ_i = 37.5 $cm^2/V{\cdot}s$ value expected from constant relaxation time approximation, suggesting a large increase in the relaxation time (τ), simultaneously with the increase in the effective mass within the HH(90%)/FH(10%) nanocomposite. The carrier mobility in all $Ti_{0.1}Zr_{0.9}Ni_{1+x}Sn$ (HH($1 - x$)/FH(x)) nanocomposites decreases almost linearly with rising temperature. An increase in the relaxation time within the $Ti_{0.1}Zr_{0.9}Ni_{1+x}Sn$ (HH($1 - x$)/FH(x)) nanocomposites can be attributed to the drop in the effective carrier density arising from the trapping at 300 K of low-energy carriers by the potential barrier, ΔE at the HH/FH interfaces (Figure 4B). Such reduction in the effective carrier density implies a reduction in the frequency of electron−electron collisions leading to a larger relaxation time between scattering events. However, this reduction in the frequency of electron−electron collisions alone does not explain why the observed carrier mobility within the HH(90%)/FH(10%) nanocomposite is 41% larger than the expected value, whereas in the HH(96%)/FH(4%) nanocomposite, the observed carrier mobility is only 16% higher than the expected value, although both HH(90%)/FH(10%) and HH(96%)/FH(4%) nanocomposites have similar carrier densities. This suggests that additional contributing factors, such as charge carrier-ionized impurity scattering and charge carrier scattering by structural defects (dislocations, vacancies), play a significant role in the alteration of the relaxation time within $Ti_{0.1}Zr_{0.9}Ni_{1+x}Sn$ (HH($1 - x$)/FH(x)) nanocomposites.

Electrical Conductivity. The above-described alterations of the magnitude and the temperature dependence of carrier density and mobility within the bulk semiconducting $Ti_{0.1}Zr_{0.9}NiSn$ (HH) matrix induced by coherently embedded FH QDs inside its atomic structure, drastically change the semiconducting behavior of the $Ti_{0.1}Zr_{0.9}Ni_{1+x}Sn$ (HH($1 - x$)/FH(x)) nanocomposites. For instance, the electrical conductivity of the $Ti_{0.1}Zr_{0.9}NiSn$ (HH) matrix decreases with rising temperature from 480 S/cm at 300 K, reaches a minimum of 320 S/cm at 680 K and increases thereafter with further increase in temperature (Figure 3C). This behavior is typical of heavily doped semiconductors in which intrinsic excitations set in at higher temperature, above about 650 K in this case. A similar trend is observed in HH(98%)/FH(2%) and HH(96%)/FH(4%) samples except that the minima in the conductivity occur at lower temperatures of 580 and 450 K, respectively. The HH(90%)/FH(10%) nanocomposite displays the intrinsic-like semiconducting behavior (σ rises with T) in the entire temperature range measured. This indicates that the nature of the carrier transport in $Ti_{0.1}Zr_{0.9}Ni_{1+x}Sn$ (HH($1 - x$)/FH(x)) nanocomposites changes from that of a heavily, extrinsic-doped semiconductor to an intrinsic semiconductor-like behavior with the increasing mole fraction of FH QDs in the $Ti_{0.1}Zr_{0.9}NiSn$ (HH) matrix. At room temperature, as a function of FH content, the electrical conductivity decreases from 480 to 370 S/cm, to 280 S/cm, and finally to 150 S/cm for 0, 2%, 4%, and 10% FH concentrations in the HH matrix, respectively. The observed drop in the electrical conductivity of $Ti_{0.1}Zr_{0.9}Ni_{1+x}Sn$ (HH($1 - x$)/FH(x)) nanocomposites at 300 K with the increasing mole fraction of FH QDs can be rationalized by the large decrease in the carrier density (Figure 3A). This gradual change of the conducting behavior toward an intrinsic semiconductor-like regime with the increasing mole fraction of the FH QDs suggests a gradual increase in the energy band gap (E_g) of the $Ti_{0.1}Zr_{0.9}Ni_{1+x}Sn$ (HH($1 - x$)/FH(x)) nanocomposites. The apparent increase in the energy band gap of $Ti_{0.1}Zr_{0.9}Ni_{1+x}Sn$ (HH($1 - x$)/FH(x)) nanocomposites and the observed changes in the carrier effective mass strongly point to profound alteration of the electronic band structure of the $Ti_{0.1}Zr_{0.9}NiSn$ (HH) matrix by the embedded FH QDs, leading to a new and fundamentally distinct material. The observed increase in the electrical conductivity of $Ti_{0.1}Zr_{0.9}Ni_{1+x}Sn$ (HH($1 - x$)/FH(x)) nanocomposites at high temperature results from the nearly

exponential increase in the carrier density and the linear decrease in the mobility with increasing temperature. This temperature dependence of the carrier density and mobility leads to a marginal (15%) decrease in the electrical conductivity of $Ti_{0.1}Zr_{0.9}Ni_{1+x}Sn$ (HH($1 - x$)/FH(x)) nanocomposites at high temperatures (Figure 3D).

Power Factor. The large enhancements (up to 200% at 300 K) of the thermopower at all temperatures and the observed minimal reduction (15%) in the electrical conductivity at high temperatures discussed above result in large improvements in the power factor (PF = σS^2) of $Ti_{0.1}Zr_{0.9}Ni_{1+x}Sn$ (HH($1 - x$)/FH(x)) nanocomposites (Figure 5B). At 300 K, the PF of the $Ti_{0.1}Zr_{0.9}NiSn$ (HH) matrix is 300 $\mu W/K^2m$ and slowly increases with temperature to 750 $\mu W/K^2m$ at 780 K. Only marginal change in the PF is observed for the HH(98%)/FH(2%) nanocomposite compared to the $Ti_{0.1}Zr_{0.9}NiSn$ (HH) matrix. Upon increasing the mole fraction of FH QDs to 4 mol %, the PF of the resulting HH(96%)/FH(4%) nanocomposite increases from 390 $\mu W/K^2m$ at 300 K to 1150 $\mu W/K^2m$ at 780 K, which corresponds to ~53% increase at 780 K when compared to the $Ti_{0.1}Zr_{0.9}NiSn$ (HH) matrix. The largest enhancement of the PF was obtained for the HH(90%)/FH(10%) nanocomposite. At 300 K, a PF value of 850 $\mu W/K^2m$ was observed. As the temperature increases, the PF of the HH(90%)/FH(10%) nanocomposite rapidly rises to a maximum value of 1960 $\mu W/K^2m$ at 780 K. This represents ~160% enhancement when compared to the PF of the $Ti_{0.1}Zr_{0.9}NiSn$ (HH) matrix. This large enhancement of the PF of the HH(90%)/FH(10%) nanocomposite at 780 K arises from the observed 70% increase in the thermopower and a marginal (15%) decrease in the electrical conductivity.

Another interesting finding in this study is the ability of the embedded FH QDs to scatter thermal phonons to reduce the thermal conductivity of the synthesized $Ti_{0.1}Zr_{0.9}Ni_{1+x}Sn$ (HH($1 - x$)/FH(x)) nanocomposites. Figure 5C shows the temperature dependence of the lattice thermal conductivity (κ_L) obtained by subtracting the electronic component κ_e from the total thermal conductivity, κ. $\kappa_e = L_o\sigma T$ was estimated using the Wiedemann−Franz law, where the Lorenz number is taken at its fully degenerate value of $L_o = 2.45 \times 10^{-8}$ W Ω K^{-2}. The lattice thermal conductivities of the $Ti_{0.1}Zr_{0.9}Ni_{1+x}Sn$ (HH($1 - x$)/FH(x)) nanocomposites at all temperatures decrease with the increasing mole fraction of the FH QDs. For instance, the lattice thermal conductivity of the $Ti_{0.1}Zr_{0.9}NiSn$ (HH) matrix at 300 K is 12.6 Wm^{-1} K^{-1} and gradually decreases to 9.05 Wm^{-1} K^{-1} for HH(90%)/FH(10%) nanocomposite (Figure 5C). This corresponds to a ~30% reduction in the lattice thermal conductivity at 300 K. Regardless of the composition, the lattice thermal conductivity monotonically decreases with increasing temperature (Figure 5C). At 775 K, the lattice thermal conductivity of $Ti_{0.1}Zr_{0.9}NiSn$ (HH) matrix decreases down to 6.56 Wm^{-1} K^{-1}, whereas that of the HH(90%)/FH(10%) nanocomposite drops to 4.75 Wm^{-1} K^{-1}, which corresponds to a 23% reduction when compared to that of the HH matrix (Figure 5C). The observed reductions in the thermal conductivities of the $Ti_{0.1}Zr_{0.9}Ni_{1+x}Sn$ (HH($1 - x$)/FH(x)) nanocomposites are attributed to the enhancement of thermal phonons scattering by the multiple nanometer scale HH/FH phase boundaries introduced by the insertion of FH QDs within the HH matrix, in addition to the mid- to long-wavelength phonons scattering at grains boundaries.[3,4,16,21]

The simultaneous large enhancements in the PF and the associated reductions in the lattice thermal conductivity of $Ti_{0.1}Zr_{0.9}Ni_{1+x}Sn$ (HH($1 - x$)/FH(x)) nanocomposites result in drastic improvements in their thermoelectric figure of merit ZT when compared to the $Ti_{0.1}Zr_{0.9}NiSn$ (HH) matrix (Figure 5D). For instance, starting with a semiconducting $Ti_{0.1}Zr_{0.9}NiSn$ (HH) matrix with ZT ~ 0.08 at 775 K, we found that coherent integration of 10 mol % of FH QDs within the crystal lattice of the semiconducting HH matrix dramatically enhances the thermoelectric performance of the resulting HH(90%)/FH(10%) nanocomposite to ZT ~ 0.28 at 775 K, a factor of 3.5 times higher ZT as compared to the $Ti_{0.1}Zr_{0.9}NiSn$ (HH) matrix.

■ CONCLUDING REMARKS

In summary, we found that QDs coherently embedded within a semiconducting matrix govern the electronic behavior of existing ensembles of charge carriers within the matrix, leading to a spectacular increase in the thermopower as well as a large enhancement in the carrier mobility within the resulting bulk nanocomposite. One plausible rationalization of the observed data can be obtained by considering that the embedded QD forms a potential barrier at the matrix/QD interface due to the offset of their CBM. This potential barrier, the height of which increases with the decreasing size of the QD, discriminates charge carriers from the conduction band of the matrix with respect to their relative energy. Therefore, carriers with energy higher than the potential barrier height (high-energy carriers) are transmitted to the CB of the QD, whereas carriers with energy lower than the potential barrier height are trapped at the matrix/QD interface and require additional thermal energy to cross the potential barrier. The above-described charge carrier culling results in a reduction of the effective carrier density within the matrix at all temperatures and in their strong temperature dependence. The simultaneous decrease in the carrier density and the increase in the carrier effective mass within the HH/FH-QD nanocomposites yield a great enhancement of their thermopower without a significant alteration of the electrical conductivity. The above results evidently demonstrate that atomic-scale crystal structure engineering of a semiconductor matrix using endotaxially embedded QDs drastically enhances the thermopower and carrier mobility in the composite material. The discovery of this novel approach to enhance thermopower and carrier mobility is expected to pave the way toward larger figures of merit in thermoelectric materials intended for high-performance energy conversion application.

■ AUTHOR INFORMATION

Corresponding Author

ppoudeup@umich.edu

Notes

The authors declare no competing financial interest.

■ ACKNOWLEDGMENTS

P.F.P.P. and C.U. gratefully acknowledge financial support from the Department of Energy, Office of Basic Energy Sciences under award no. DE-SC-0008574. S.-J. K. and X.P. acknowledge support of the Center for Solar and Thermal Energy Conversion, an Energy Frontier Research Center funded by the U.S. Department of Energy, Office of Science, Office of Basic Energy Sciences under award no. DE-SC0000957 (contributions in TEM studies). This work made use of the JEOL 3011 High Resolution Electron Microscope from the Michigan's

Materials Characterization Facility-EMAL (Electron Microbeam Analysis Laboratory), purchased with funds from the National Science Foundation (award no. DMR-0315633).

■ REFERENCES

(1) Vineis, C. J.; Shakouri, A.; Majumdar, A.; Kanatzidis, M. G. *Adv. Mater.* **2010**, *22*, 3970.
(2) Snyder, G. J.; Toberer, E. S. *Nat. Mater.* **2008**, *7*, 105.
(3) Biswas, K.; He, J. Q.; Zhang, Q. C.; Wang, G. Y.; Uher, C.; Dravid, V. P.; Kanatzidis, M. G. *Nat. Chem.* **2011**, *3*, 160.
(4) Kanatzidis, M. G. *Chem. Mater.* **2010**, *22*, 648.
(5) Sootsman, J. R.; Chung, D. Y.; Kanatzidis, M. G. *Angew Chem., Int. Ed.* **2009**, *48*, 8616.
(6) Poudeu, P. F. P.; D'Angelo, J.; Downey, A. D.; Short, J. L.; Hogan, T. P.; Kanatzidis, M. G. *Angew Chem., Int. Ed.* **2006**, *45*, 3835.
(7) Hsu, K. F.; Loo, S.; Guo, F.; Chen, W.; Dyck, J. S.; Uher, C.; Hogan, T.; Polychroniadis, E. K.; Kanatzidis, M. G. *Science* **2004**, *303*, 818.
(8) Poudel, B.; Hao, Q.; Ma, Y.; Lan, Y. C.; Minnich, A.; Yu, B.; Yan, X.; Wang, D. Z.; Muto, A.; Vashaee, D.; Chen, X. Y.; Liu, J. M.; Dresselhaus, M. S.; Chen, G.; Ren, Z. *Science* **2008**, *320*, 634.
(9) Heremans, J. P.; Jovovic, V.; Toberer, E. S.; Saramat, A.; Kurosaki, K.; Charoenphakdee, A.; Yamanaka, S.; Snyder, G. J. *Science* **2008**, *321*, 554.
(10) Pei, Y. Z.; Shi, X. Y.; LaLonde, A.; Wang, H.; Chen, L. D.; Snyder, G. J. *Nature* **2011**, *473*, 66.
(11) Makongo, J. P. A.; Misra, D. K.; Zhou, X. Y.; Pant, A.; Shabetai, M. R.; Su, X. L.; Uher, C.; Stokes, K. L.; Poudeu, P. F. P. *J. Am. Chem. Soc.* **2011**, *133*, 18843.
(12) Tritt, T. M.; Bottner, H. *J. Mater. Res.* **2011**, *26*, 1743.
(13) Harman, T. C.; Taylor, P. J.; Walsh, M. P.; LaForge, B. E. *Science* **2002**, *297*, 2229.
(14) Venkatasubramanian, R.; Siivola, E.; Colpitts, T.; O'Quinn, B. *Nature* **2001**, *413*, 597.
(15) Poudeu, P. F.; Salvador, J.; Sakamoto, J. *Sci Adv Mater* **2011**, *3*, 515.
(16) Makongo, J. P. A.; Misra, D. K.; Salvador, J. R.; Takas, N. J.; Wang, G.; Shabetai, M. R.; Pant, A.; Paudel, P.; Uher, C.; Stokes, K. L.; Poudeu, P. F. P. *J. Solid State Chem.* **2011**, *184*, 2948.
(17) Chai, Y. W.; Kimura, Y. *Appl. Phys. Lett.* **2012**, *100*, 033114.
(18) Populoh, S.; Aguirre, M. H.; Brunko, O. C.; Galazka, K.; Lu, Y.; Weidenkaff, A. *Scr. Mater.* **2012**, *66*, 1073.
(19) Sumithra, S.; Takas, N. J.; Nolting, W. M.; Sapkota, S.; Poudeu, P. F. P.; Stokes, K. L. *J. Electron. Mater.* **2012**, *41*, 1401.
(20) Zhao, L.-D.; He, J.; Hao, S.; Wu, C.-I.; Hogan, T. P.; Wolverton, C.; Dravid, V. P.; Kanatzidis, M. G. *J. Am. Chem. Soc.* **2012**, *134*, 16327.
(21) Biswas, K.; He, J.; Blum, I. D.; Wu, C.-I.; Hogan, T. P.; Seidman, D. N.; Dravid, V. P.; Kanatzidis, M. G. *Nature* **2012**, *489*, 414.
(22) Jeitschko, W. *Metall. Trans.* **1970**, *1*, 3159.
(23) Webster, P. J.; Ziebeck, K. R. A. *Landolt-Börnstein-group III condensed matter*; Berlin: Springer, 1988; Vol. *19C*.
(24) Misra, D. K.; Makongo, J. P. A.; Sahoo, P.; Shabetai, M. R.; Paudel, P.; Stokes, K. L.; Poudeu, P. F. P. *Sci. Adv. Mater.* **2011**, *3*, 607.
(25) Takas, N. J.; Sahoo, P.; Misra, D.; Zhao, H. F.; Henderson, N. L.; Stokes, K.; Poudeu, P. F. P. *J. Electron. Mater.* **2011**, *40*, 662.
(26) Yaqub, R.; Sahoo, P.; Makongo, J. P. A.; Takas, N.; Poudeu, P. F. P.; Stokes, K. L. *Sci. Adv. Mater.* **2011**, *3*, 633.
(27) Culp, S. R.; Simonson, J. W.; Poon, S. J.; Ponnambalam, V.; Edwards, J.; Tritt, T. M. *Appl. Phys. Lett.* **2008**, *93*, 022105.
(28) Poon, S. J. In *Semiconductor and Semimetals*; Tritt, T. M., Ed.; Academic: New York, 2001; Vol. *70*, p 37.
(29) Aliev, F. G.; Brandt, N. B.; Moshchalkov, V. V.; Kozyrkov, V. V.; Skolozdra, R. V.; Belogorokhov, A. I. *Z. Phys. B: Condens. Matter* **1989**, *75*, 167.
(30) Aliev, F. G.; Kozyrkov, V. V.; Moshchalkov, V. V.; Scolozdra, R. V.; Durczewski, K. *Z. Phys. B: Condens. Matter* **1990**, *80*, 353.
(31) Simonson, J. W.; Poon, S. J. *J. Phys.: Condens. Matter* **2008**, *20*, 255220.
(32) Barth, J.; Balke, B.; Fecher, G. H.; Stryhanyuk, H.; Gloskovskii, A.; Naghavi, S.; Felser, C. *J. Phys. D: Appl. Phys.* **2009**, *42*, 185401.
(33) Chaput, L.; Tobola, J.; Pecheur, P.; Scherrer, H. *Phys. Rev. B* **2006**, *73*, 045121.
(34) Sakurada, S.; Shutoh, N. *Appl. Phys. Lett.* **2005**, *86*, 082105.
(35) Uher, C.; Yang, J.; Hu, S.; Morelli, D. T.; Meisner, G. P. *Phys. Rev. B* **1999**, *59*, 8615.
(36) Nanda, B. R. K.; Dasgupta, I. *J. Phys.: Condens Matter* **2005**, *17*, 5037.
(37) Kroth, K.; Balke, B.; Fecher, G. H.; Ksenofontov, V.; Felser, C.; Lin, H. J. *Appl. Phys. Lett.* **2006**, *89*, 202509.
(38) Ouardi, S.; Fecher, G. H.; Balke, B.; Kozina, X.; Stryganyuk, G.; Felser, C.; Lowitzer, S.; Kodderitzsch, D.; Ebert, H.; Ikenaga, E. *Phys. Rev. B* **2010**, *82*, 085108.
(39) Sanyal, B.; Eriksson, O.; Suresh, K. G.; Dasgupta, I.; Nigam, A. K.; Nordblad, P. *Appl. Phys. Lett.* **2006**, *89*, 212502.
(40) Lin, H.; Wray, L. A.; Xia, Y. Q.; Xu, S. Y.; Jia, S. A.; Cava, R. J.; Bansil, A.; Hasan, M. Z. *Nat. Mater.* **2010**, *9*, 546.
(41) Chadov, S.; Qi, X. L.; Kubler, J.; Fecher, G. H.; Felser, C.; Zhang, S. C. *Nat. Mater.* **2010**, *9*, 541.
(42) Xiao, D.; Yao, Y. G.; Feng, W. X.; Wen, J.; Zhu, W. G.; Chen, X. Q.; Stocks, G. M.; Zhang, Z. Y. *Phys. Rev. Lett.* **2010**, *105*, 096404.
(43) Graf, T.; Felser, C.; Parkin, S. S. P. *Prog. Solid State Chem.* **2011**, *39*, 1.
(44) *Heavily Doped Semiconductors*; Fistul, V. I., Ed.; Plenum: New York, 1969.
(45) Ravich, Y. I.; Efimova, B. A.; Smirnov, I. A.; *Semiconducting Lead Chalcogenides*; Stilbans, L. S., Ed.; Plenum. Press: New York-London, 1970.